



Decomposition of formic acid over silica encapsulated and amine functionalised gold nanoparticles

Mielby, Jerrik Jørgen; Kunov-Kruse, Andreas Jonas; Kegnæs, Søren

Published in:
Journal of Catalysis

Link to article, DOI:
[10.1016/j.jcat.2016.11.020](https://doi.org/10.1016/j.jcat.2016.11.020)

Publication date:
2017

Document Version
Peer reviewed version

[Link back to DTU Orbit](#)

Citation (APA):

Mielby, J. J., Kunov-Kruse, A. J., & Kegnæs, S. (2017). Decomposition of formic acid over silica encapsulated and amine functionalised gold nanoparticles. *Journal of Catalysis*, 345, 149-156. DOI: 10.1016/j.jcat.2016.11.020

General rights

Copyright and moral rights for the publications made accessible in the public portal are retained by the authors and/or other copyright owners and it is a condition of accessing publications that users recognise and abide by the legal requirements associated with these rights.

- Users may download and print one copy of any publication from the public portal for the purpose of private study or research.
- You may not further distribute the material or use it for any profit-making activity or commercial gain
- You may freely distribute the URL identifying the publication in the public portal

If you believe that this document breaches copyright please contact us providing details, and we will remove access to the work immediately and investigate your claim.

Decomposition of formic acid over silica encapsulated and amine functionalised gold nanoparticles

Jerrik Mielby, Andreas Jonas Kunov-Kruse and Søren Kegnæs*

DTU Chemistry, Technical University of Denmark, Kemitorvet 207, DK-2800 Kgs. Lyngby, Denmark.
skk@kemi.dtu.dk

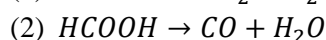
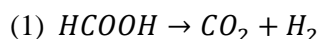
Abstract

Formic acid has recently attracted considerable attention as a safe and convenient source of hydrogen for sustainable chemical synthesis and renewable energy storage. Here, we show that silica encapsulated and amine functionalised gold nanoparticles are highly active catalysts for the production of hydrogen by vapour phase decomposition of formic acid. The core-shell catalysts are prepared in a reverse micelle system that makes it possible to control the size of the Au nanoparticles and the thickness of the SiO₂ shells, which has a large impact on the catalytic activity. The smallest gold nanoparticles are 2.2 ± 0.3 nm in diameter and have a turnover frequency (TOF) of up to 958 h⁻¹ at a temperature of 130°C. Based on detailed *in situ* ATR-FTIR studies and results from kinetic isotope labelling experiments we propose that the active site is a low-coordinated and amine functionalised Au atom, while H-assisted formate decomposition into CO₂ and H₂ is the rate limiting step.

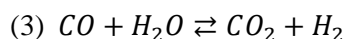
1 Introduction

Hydrogen produced from renewable resources holds great promise for sustainable production of chemicals and clean energy. Unfortunately, the physical properties of hydrogen gas make transportation, handling and refuelling difficult. Formic acid (HCOOH) has great potential as a hydrogen storage material and as a means to utilise CO₂ [1]. Furthermore, formic acid may be produced directly from biomass, for instance by the catalytic oxidation of cellulose using heteropoly acids [2]. In general, the decomposition of formic

acid may occur via dehydrogenation (1) or dehydration (2)



The two reactions pathways are linked by the well-known water-gas shift reaction (3)



From the perspective of energy storage, the production of pure H₂ remains an important challenge because even small amount of CO severely deactivate the platinum in fuel cell catalysts. Alternatively, the efficient activation of formic acid may be exploited for transfer hydrogenations in organic synthesis [3].

Supported gold nanoparticles have recently attracted much attention because of their surprisingly high catalytic activity for a number of reactions [4–6], in particular CO oxidation [7]. Although the intimate mechanistic details are still not fully understood, it is generally accepted that several factors contribute to the high activity [8]. In particular, the gold nanoparticles must typically be less than 10 nm in diameter so that under-coordinated, reactive gold atoms exist in large numbers at the edges and corners of the particles [9]. Supported gold nanoparticles have also previously been used to decompose formic acid in both liquid [10,11] and vapour phase [12–15]. Ojeda and Iglesia [12] showed that highly dispersed gold catalysts decomposed formic acid with higher metal-time yields than similar Pt catalysts in vapour phase. The authors suggested

that the high catalytic activity was caused by disperse Au species (undetectable by TEM) and not from visible metal nanoparticles (3-4 nm), which were active for CO oxidation and remained stable during thermal treatment. The decomposition of formic acid has also been investigated by means of periodic density functional theory calculations [16,17]. In particular, Yoo *et al.* [17] studied the reaction on Ag, Cu, Pd and Pt. The study was extended to other transition-metals by scaling the adsorption energies of the involved reaction species with two independent descriptors, namely the CO and OH adsorption energies. Small Au clusters of 0.8 nm in diameter (13 Au atoms) were found to bind CO and OH more strongly than bulk gold, which brought the activity of Au very close to the top of the volcano plot. The small Au clusters were even found to be more active and selective than Pt, which is in good agreement with the results reported by Ojeda and Iglesia [12].

Here, we demonstrate that gold nanoparticles encapsulated in silica are highly effective catalysts for the vapor phase decomposition of formic acid under mild conditions. The catalysts are prepared by means of the reverse micelle methodology recently reported by Zhang *et al.* [18]. In this approach, the gold precursor is first precipitated with an aqueous solution of ammonia and then subjected to a controlled silica coating in a reverse micelle system comprised of a commercial surfactant (Brij-10) in cyclohexane. Furthermore, the method takes advantage of a the strong interactions between gold and (3-aminopropyl)trimethoxysilane (APTMS), which gives a good control over the size and encapsulation of the Au nanoparticles. The smallest and most active gold nanoparticles were 2.2 ± 0.3 nm in diameter and decomposed formic acid with a turnover frequency (TOF) of up to 958 h^{-1} at a temperature of 130°C . To the best of our knowledge, these are the first detailed studies of the decomposition of pure formic acid over silica encapsulated Au nanoparticles in vapour phase, although Yadav *et al.* previously reported good results for the decomposition of sodium formate and formic acid

mixtures in liquid phase using a similar catalyst design [11]. Based on *in situ* ATR-FTIR spectroscopy and results from kinetic isotope labelling experiments we propose that the active site is a low-coordinated and amine functionalised Au atom, while the formation of H_2 is the rate limiting step.

2 Experimental section

2.1 General synthesis

The Au@SiO₂ core-shell catalysts were prepared according to a modified literature procedure [18]. In a typical synthesis, 4.25 g of Brij C10 was dissolved in 7.5 mL of cyclohexane at 50°C . Then, 0.5 ml of HAuCl₄ (0.25 M) was added dropwise under stirring, followed by 0.8 ml of aqueous NH₃ (25%), 150 μl APTMS and 2 ml of tetraethyl orthosilicate (TEOS), which were added in order with intervals of 2 min. The hydrolysis and condensation of TEOS was allowed to proceed for 2 hours at 50°C followed by stirring overnight with no heating. The product was collected by centrifugation, washed with ethanol, dried at 80°C and then reduced under hydrogen gas (10% H_2 in N_2) for 2 h at 200°C using a heating ramp of $5^\circ\text{C}/\text{min}$. In order to investigate the effect of the size of the Au nanoparticles and the thickness of the SiO₂ shells, we prepared three other catalysts by increasing the amount of cyclohexane (15 ml), decreasing the concentration of HAuCl₄ (0.125 M) and increasing the amount of TEOS (4 ml), respectively. Furthermore, we prepared one catalysts comprised of pure SiO₂.

2.2 Catalytic tests

The vapour phase decomposition of HCOOH was performed at atmospheric pressure in a 3 mm quartz fixed-bed reactor. The formic acid was introduced to the reactor by bubbling Ar (40 ml/min) through pure formic acid kept in a thermostatic bath at 20°C , which resulted in gas composition of around 7% formic acid. The reaction gas was preheated to the reaction temperature and then passed through the reactor,

which contained the fractionated catalyst (180–355 μm). The amount of catalyst (50–100 mg) was adjusted to the Au loading in order to have a constant weight hourly space velocity (WHSV) of around 138 g formic acid/g Au hour⁻¹. The reaction products, which were either CO₂ and H₂ or CO and H₂O, were quantified with an online Rosemount BINOS 100 non-dispersive infrared (NDIR) detector that followed the formation of CO and CO₂ as function of the reaction temperature as measured inside the reactor. The formation of other important products (in particular H₂) was followed by an online Pfeiffer Vacuum ThermoStar mass spectrometer (MS). All catalysts were tested under the same reaction condition using a preprogrammed heating profile going from 20–200°C and then back to 20°C by 2°C/min. All kinetic data was collected after the temperature had reached 200°C. The kinetic isotope effect was investigated by replacing HCOOH with HCOOD, DCOOH and DCOOD, respectively.

2.3 *In situ* ATR-FTIR spectroscopy

The reaction mechanism was investigated using a Thermo Fisher iS50 Fourier transformation infrared (FTIR) instrument with a Specac high-temperature Golden Gate diamond attenuated total reflectance (ATR) accessory, which could heat the sample area up to 300°C. A custom build flow cell allowed the catalyst to be studied under reaction conditions by *in situ* ATR-FTIR. The catalyst was gently pressed into a wafer and mounted in the ATR flow cell using an inner piston, which pressed the catalyst against the ATR-diamond to ensure intimate contact, while the formic acid vapour was passed over it. A schematic drawing of the setup is given in the supporting information (Figure S10). Further details, descriptions and drawings of the environmental ATR-FTIR device and the concept behind it can be found elsewhere [19].

All *in situ* ATR-FTIR experiments was performed at 120°C. Before exposure to formic acid, the catalyst was first dried in a flow of dry nitrogen (25 ml/min) for around 1 hour at the same temperature.

The procedure for the *in situ* experiments with DCOOD was similar to the experiments described above. However, to exchange mobile protons on the amine species, and thus make the interpretation more straightforward, the catalyst was first stirred in D₂O for 48 h at 100°C. The D₂O treated catalyst was then dried in an oven prior to the preparation for ATR-FTIR analysis. The enrichment procedure did, however, not result in a complete exchange of the mobile protons.

2.4 Computational methods

Assignments of vibrational modes were carefully performed in a combination of density functional theory (DFT) calculations and reference experiments with deuterated formic acid. The DFT calculations were performed using the BP86 functional with the TZVP basis set in Gaussian09. No scaling factor was applied for the calculated spectra. Silica surface was simulated with a small H₃Si₄O₆-OH unit, which despite its simplicity, is known to give good results for studies of vibrational modes [20]. Silica grafted propyl amine was simulated using the analogous H₃Si₄O₆-(CH₂)₃NH₂. Screenshots of the structures and selected vibrational modes are shown in the supporting information Figure S11. An overview of relevant spectral assignments and approximate modes are also given in supporting information Scheme S1.

3 Results and discussion

3.1 Characterization

Figure 1 shows two representative TEM images of the Au@SiO₂ core-shell catalyst as prepared by the general synthesis described in section 2.1. The image shows how the individual Au nanoparticles were uniformly encapsulated in small spheres of SiO₂ with a shell thickness of 8–12 nm. TEM images of all the prepared catalysts are shown in the supporting information.

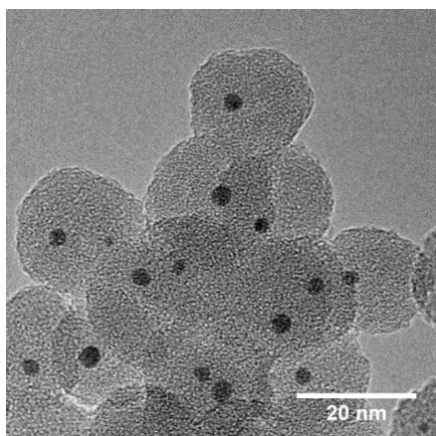


Figure 1. TEM image of the Au@SiO₂ 2.8±0.5 core-shell catalyst.

The TEM image in Figure 1 is in good agreement with the results from X-ray diffraction (XRD) analysis shown in the supporting information (Figure S1). The diffraction pattern shows no clear peaks from the core-shell catalyst since the SiO₂ shells were amorphous and the Au cores were relatively small (2.8±0.5 nm). The weak diffraction peaks at $2\theta=38, 44, 65$ and 78 were assigned to Au(111), Au(200), Au(220) and Au(311), respectively, in good agreement with bulk gold. In general, the peaks are too weak to estimate the size of the nanoparticles by line broadening analysis.

The surface area and pore volume were investigated by nitrogen physisorption analysis performed at 77 K. The physisorption isotherm in Figure 2 shows a significant hysteresis loop, which corresponds to an average pore size distribution of around 11 nm as determined by BJH-analysis of the isotherm desorption branch (see Figure S2 in the supporting information). The pore size distribution is in good agreement with the expected porosity related to the inter-particle voids that exists between the individual spherical particles. From the small amount of N₂ that adsorbed at low partial pressures, the isotherm also shows that the silica shells had very limited porosity in the microporous range (<2 nm). A single point read at $p/p^0=0.99$ resulted in a total pore volume of 0.57 cm³/g, while BET analysis resulted in a total surface area of 203 m²/g.

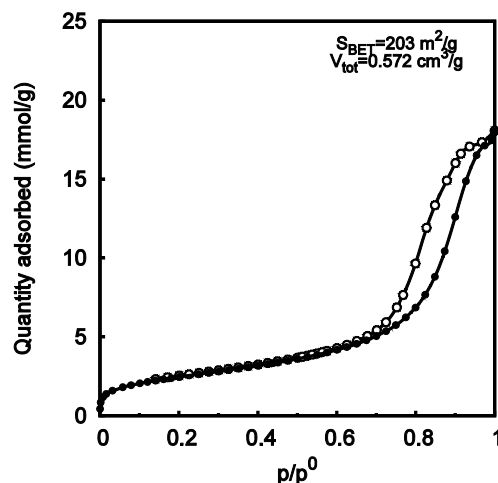


Figure 2. N₂ physisorption isotherm of the Au@SiO₂ 2.8±0.5 catalyst.

Figure 3 shows the Au nanoparticle size distribution of four different catalysts prepared using the reverse micelle method. The catalysts are denoted by Au@SiO₂ followed by the average size and standard deviation in nm. The particle size distributions of the Au nanoparticles were calculated from the measurement of around 300 nanoparticles by TEM. Figure 3a shows the particle size distribution of the typical catalyst with a metal loading of 4.4 wt% Au and an average size of 2.8±0.5 nm. The catalyst was prepared using 7.5 ml of cyclohexane, 0.5 ml 0.25 M HAuCl₄ and 2.0 ml tetraethyl orthosilicate (TEOS) according to section 2.1. By increasing the amount of cyclohexane to 15 ml we were able to decrease the average particle size from 2.8±0.5 nm to 2.6±0.3 nm, see Figure 3b. By decreasing the amount of gold to 0.5 ml 0.125 M HAuCl₄ (2.2 wt% Au) we were further able to decrease the average particle size to 2.2±0.3 nm, see Figure 3c. In general, the diluted system resulted in more narrow size distributions. We also tried to increase the shell thickness by increasing the amount of TEOS to 4 ml. Figure 3d shows how the increased amount of TEOS decreased the average size of the Au nanoparticles to 2.7±0.4 nm. The small decrease in size and corresponding increase in the total number of particles caused the shell thickness to increase slightly less than expected from simple geometric

calculations. While the general 4.4 wt% Au@SiO₂ 2.8±0.5 catalyst (A) had an average shell thickness of 21.9±2.0 nm, the 2.2 wt% Au@SiO₂ 2.7±0.4 catalyst (D) had an average shell thickness of

26.2±1.9 nm. Further attempts to decrease the shell thickness by adding less TEOS without increasing the size of the Au nanoparticles were not successful.

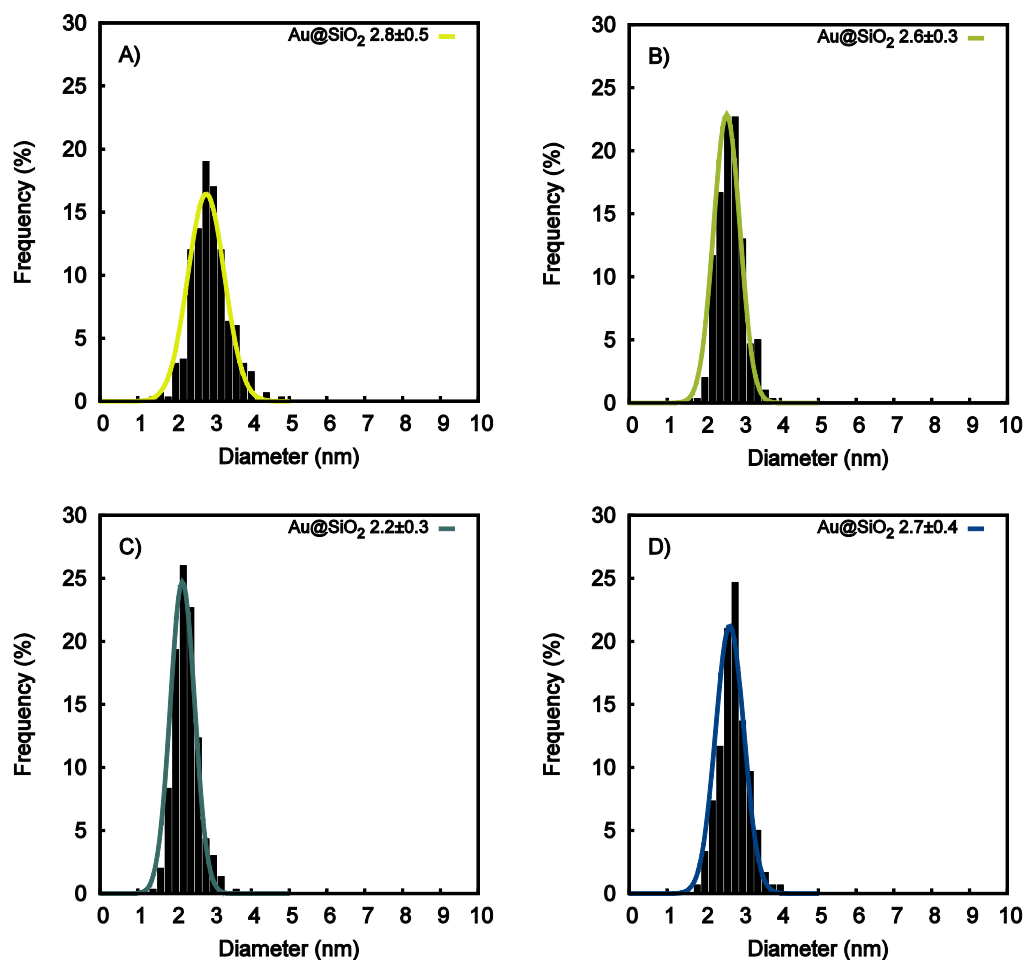


Figure 3. Au nanoparticle size distribution of the four core-shell catalysts.

3.2 Catalytic activity

Figure 4 show the conversion of HCOOH as function of the temperature. Since the total amount of Au was kept constant in all catalytic experiments the catalytic activity can be directly compared by the temperature at 50% conversion. While the core-shell catalyst with the largest Au nanoparticles (2.8±0.5 nm) reached 50% HCOOH conversion at a temperature of 132°C, the catalyst with slightly smaller nanoparticles (2.6±0.3 nm) reached 50%

conversion at 128°C. The catalyst with the smallest Au nanoparticles (2.2±0.3 nm) had a significantly higher activity and already reached 50% conversion at 119°C. The catalyst with increased SiO₂ shell thickness was less active than the other catalysts and only resulted in 50% conversion at 140°C.

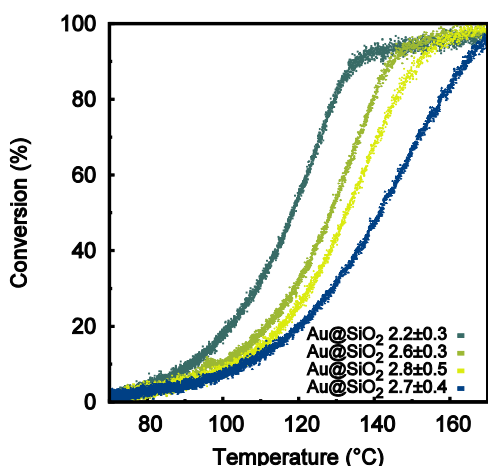


Figure 4. Light-off curve for the conversion of HCOOH as function of the reaction temperature.

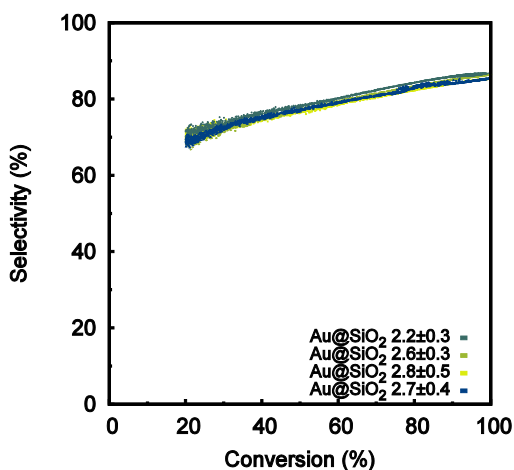


Figure 5. Selectivity towards H_2 and CO_2 as function of the conversion of HCOOH .

Figure 5 shows the selectivity towards H_2 and CO_2 as function of the conversion in the same experiments (above 20% conversion for clarity). The data show that the smallest gold nanoparticles resulted in slightly better selectivity toward H_2 . We speculate that the relatively small difference in

selectivity may be explained by the thermodynamic equilibrium, which favours the formation of CO_2 and H_2 over CO and H_2O at lower temperatures. In general, all catalysts reached around 85-87% selectivity at full conversion, which is lower than in liquid phase (up to 100%) [10,11], but significantly higher than previously reported for *e.g.* Au/TiO_2 in vapour phase (70%) [13]. Although Al_2O_3 previously has been shown to favour dehydration [14], a recent study of different metal oxide support reports high selectivity for $\text{Au/Al}_2\text{O}_3$ (>99%) [21].

Table 1 shows a summary of the prepared catalysts, their average particle size distribution and catalytic activity. The turnover frequency (TOF) was determined from the H_2 yield and the Au dispersion, and are given in mol H_2 per mol of surface Au atoms per hour at 130°C . The Au dispersion D (*i.e.* the surface-to-volume atomic ratio) was calculated from the average particle size (d) by the relation $D=1.16/d$, assuming equal proportions of the three low-index planes (111), (100) and (110) on the surface of a spherical face-centered cubic Au particle [22]. The calculated TOFs shows the remarkable effect that the size has on the intrinsic activity of Au nanoparticles. Since it previously has been shown that the relative number of low-coordinated Au corner atoms increases significantly around 2 nm [23,24], we speculate that these sites may play an important role in the decomposition of formic acid.

Entry C in Table 1 show that the smallest gold nanoparticles resulted in a TOF of 958 h^{-1} at 130°C . For comparison, Gazsi *et al.* [14] previously reached a TOF of around 692 h^{-1} using Au/SiO_2 prepared by deposition-precipitation under similar reaction conditions.

Table 1. Outline of the prepared catalysts, their average particles size distributions, catalytic activity and apparent activation energies.

Entry	Catalyst	Au loading (wt%)	Au size (nm)	SiO ₂ size (nm)	Au dispersion (D=1.16/d)	TOF ^a at 130°C (h ⁻¹)	E _a (kJ/mol)
A	Au@SiO ₂	4.4	2.8±0.5	21.9±2.0	0.41	488	70
B	Au@SiO ₂	4.4	2.6±0.3	20.2±1.3	0.45	627	68
C	Au@SiO ₂	2.2	2.2±0.3	21.1±1.6	0.53	958	71
D	Au@SiO ₂	2.2	2.7±0.4	26.2±1.9	0.43	421	61
E	SiO ₂	n/a	n/a	34.2±2.2	n/a	no activity	n/a

^a The turnover frequencies are given in mol H₂ per mol of surface Au atoms per hour at 130°C.

Figure 6 shows the Arrhenius plots based on the four light-off curves in Figure 4 from around 15-60% conversion. The apparent activation energies E_a (as obtained from the slope of the Arrhenius plots) were around 68-71 kJ/mol, which are up to 18 kJ/mol higher than for highly dispersed Au/Al₂O₃ as reported by Ojeda [12]. Furthermore, the activation energy of the catalyst with increased shell thickness was only 61 kJ/mol. The lower activation energy indicates that the diffusion of formic acid through the silica shell may limit the reaction rate, which shows that both the Au nanoparticle size distribution and the SiO₂ shell thickness have a large impact on the catalytic activity.

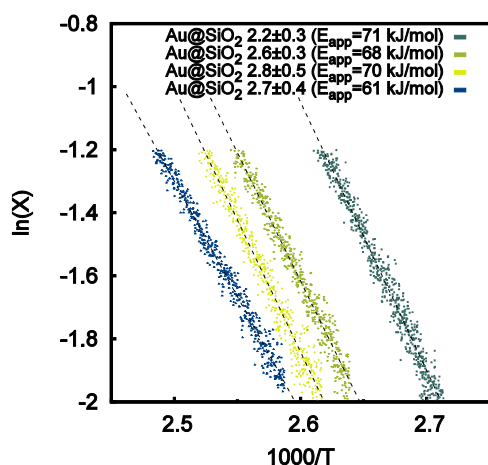


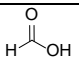
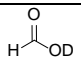
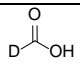
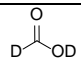
Figure 6. Arrhenius plot for the decomposition of formic acid over the prepared catalysts.

3.3 Kinetic isotope effect

The nature of the reaction was further investigated by means of the H/D kinetic isotope effect (KIE). If the dissociation of the acidic H atom is rate limiting for the decomposition of HCOOH, the KIE would be expected to give normal values (*i.e.* $r_H/r_D > 1$) for HCOOD, but not for DCOOH. Similarly, rate limiting formate decomposition would give normal values for DCOOH, but not for HCOOD, while rate limiting formation of H₂ would give normal values for both HCOOD and DCOOH [12].

With the Au@SiO₂ 2.8±0.5 catalysts all isotopomers resulted in normal KIE-values, see Table 2. The values were of apparent kinetic origin since no significant HCOOD/DCOOH scrambling was observed under the given reaction conditions. The values were, however, slightly lower than previously reported in the literature [12,10]. We suggest that the lower KIE-values may be explained by internal diffusion limitations, which appeared to be rate limiting. Further efforts to increase the diffusion by decreasing the shell thickness or increasing the porosity are therefore currently undertaken in our lab.

Table 2. Kinetic isotope effect for the vapour phase decomposition of formic acid over Au@SiO₂ 2.8±0.5 at 140 °C.

Isotopomer				
KIE= r_H/r_D	1.0	1.7	1.9	4.1

As expected, the decomposition of HCOOH and DCOOD resulted in 100% H₂ and D₂, respectively. However, in contrast to previous results from liquid phase experiments, we found that switching the substrate to HCOOD and DCOOH resulted in a distribution of both H₂, HD and D₂. It is important to underline that these results does not question that the decomposition of formic acid is a unimolecular reaction [12], but simply indicate that recombinative hydrogen desorption or water-gas shift may scramble the hydrogen isotopomers under the given reaction conditions.

3.4 Mechanistic studies

Although all kinetic data were collected after the temperature had reached 200°C, we found that the catalytic activity was higher during the initial heating ramp, while subsequent cooling and heating cycles resulted in a similar light-off curve, see supporting information Figure S8. TEM analysis of the used catalyst resulted in the same particle size distribution (2.2±0.3 nm), which indicated that no significant sintering occurred under the given reaction conditions. Moreover, the slope of the corresponding Arrhenius plot in Figure S9 did not indicate any changes in the diffusion or reaction mechanism. This indicated that the decrease in activity was more likely caused by a partial chemical deactivation such as *e.g.* substrate poisoning.

In order to investigate the partial deactivation in more detail, we performed a series of *in situ* Fourier transform infrared (FTIR) spectroscopy experiments using a custom build flow reactor that allowed the active catalyst to be studied under reaction conditions by attenuated total reflection

(ATR). A detailed description of the ATR-FTIR reactor is given in the supporting information.

After drying in a flow of N₂, the most distinctive features of the pure SiO₂ sample (Table 1, entry 5) could be assigned to the typical modes of silica with well resolved bands at 795, 950 and 1045 cm⁻¹, together with a range of intense but overlapping bands from 1120-1280 cm⁻¹ [20] (see supporting information S12). Especially the band at around 1045 cm⁻¹ due to transverse optic Si-O stretching modes, ν_{Si-O} , were very intense [20,25]. The pure silica samples showed a rather weak but well-resolved ν_{Si-OH} stretching band at around 3700 cm⁻¹. Even at 120°C physisorbed water was present as evident by the broad ν_{HOH} band peaking at around 3500-3400 cm⁻¹ as well as by the weak but well resolved OH bending band at around 1600-1650 cm⁻¹. Weak traces of the partly decomposed surfactant used in the synthesis were observed in the form of very weak C-H bands (3000-2800cm⁻¹) as well as a weak band at around 1575 cm⁻¹. The amine-free SiO₂ sample was then exposed to HCOOH in N₂ at 120°C, which showed that the formic acid was physisorbed on the surface in its protonated form, most probably by hydrogen bonding to the Si-OH groups (DFT structures and full spectra are shown in the supporting information Figure S11(b) and S13). As expected, the physisorbed species were desorbed again when the sample was flushed with pure N₂.

The amine containing Au@SiO₂ 2.2±0.3 core-shell catalyst (entry 3 in) was first investigated at 120°C in a flow of N₂ (supporting information S12) and then in a flow of HCOOH in N₂ (Figure 7(a) and supporting information Figure S13-S14). In a similar manner, the catalyst was also exposed to DCOOD, see Figure 7(b). Due to the larger mass of deuterium, modes involving stretching or bending of deuterium normally shifts downwards. In some cases, such as *e.g.* partially exchange, new modes also appear due to change of symmetry. Figure S11 and Scheme S1 in the supporting information show the structure of the relevant deuterated species as simulated by DFT.

In general, the spectra of the Au@SiO_2 2.2 ± 0.3 catalyst showed the same characteristic features as the pure SiO_2 sample. Furthermore, the spectra also revealed the presence of the silane grafted propylamine, which was added in the form of APTMS during the synthesis. The most distinctive features of the propylamine species were the N-H

stretching band (ν_{NH}) peaking at around 3300-3200 cm^{-1} as well as an aliphatic $\nu_{\text{C-H}}$ and $\delta_{\text{C-H}}$ bands at around 3000-2900 cm^{-1} and 1350-1450 cm^{-1} , respectively, and a δ_{NH} band at around 1590-1650 cm^{-1} slightly overlapping with the δ_{OH} band from water (1640 cm^{-1}).

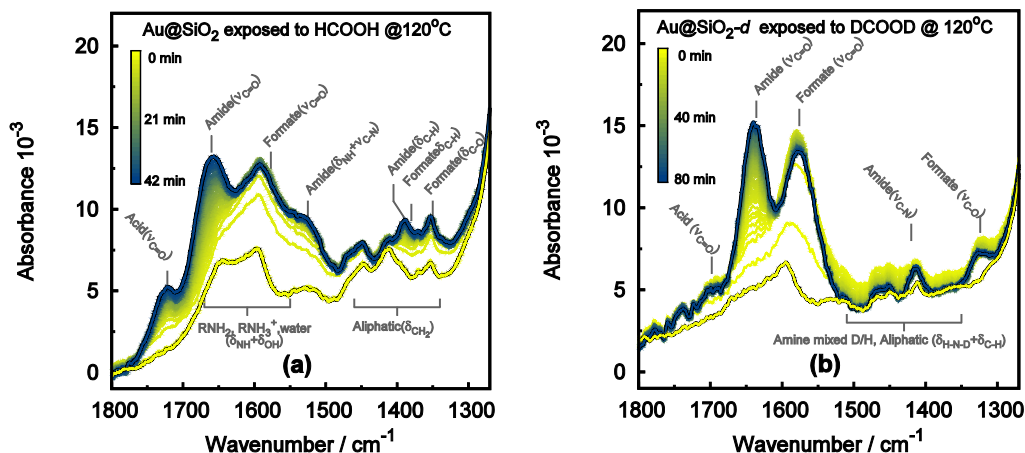


Figure 7. In situ ATR-FTIR spectra recorded at 120°C on the Au@SiO_2 2.2 ± 0.3 core-shell catalyst. The spectra are coloured with a gradient indicating time of exposure. Initial yellow spectrum, are indicated with a black line for clarity. a) The pre-dried catalyst being exposed to formic acid vapours in N_2 . b) Deuterium enriched (48 h in D_2O at 100°C) and pre-dried Au@SiO_2 2.2 ± 0.3 catalyst being exposed to formic acid- d_2 vapours in N_2 . Selected assignments are shown.

The spectra changed rapidly as soon as the catalyst was exposed to HCOOH ($t = 0$ min indicates the time for introducing HCOOH). Most notably, an intense $\nu_{\text{C=O}}$ band was formed at 1577 cm^{-1} , which clearly showed that the main part of the adsorbed formic acid was deprotonated. This was in direct contrast to the sample of pure SiO_2 , although a small amount of physisorbed formic acid was also evident on the Au@SiO_2 2.2 ± 0.3 catalyst ($\nu_{\text{O-C-O}}$ at 1720 cm^{-1}). The intense carboxylate band at 1577 cm^{-1} was shouldered to both sides by various δ_{NH_3} and δ_{NH_2} modes from the ammine/ammonium absorbing in the same region. Furthermore, two bands also appeared at 1380 and 1360 cm^{-1} , which were assigned to the formate $\delta_{\text{C-H}}$ and symmetric $\nu_{\text{C-O}}$, respectively. In general, the adsorption and

formation of ammonium formate species was relatively fast and approached steady state after a few minutes with both HCOOH and DCOOD .

The carboxylate band appeared even sharper during DCOOD absorption with no neighboring amine bands or shoulders. We believe that this is because the ND modes of the fully deuterated amine is shifted below 1200 cm^{-1} . In the beginning, however, some mixed N-(D/H) bending appeared in the 1500-1350 cm^{-1} region as broad and poorly resolved peaks. The deuterium exchange of the amines was further evident from the NH stretching modes at around 3400-3200 cm^{-1} , which was shifted downward to around 2530-2450 cm^{-1} (see

full range spectrum in supporting information Figure S15).

After the bands associated with ammonium formate species reached steady state, a new intense band slowly started to appear at 1665 cm^{-1} (1635 cm^{-1} for the DCOOD experiment). After further exposure, the intensity of the 1577 cm^{-1} band seemed to decrease slightly with the formation of the species associated with the 1665 cm^{-1} band. We assigned the latter band to amide species formed between the grafted amines and formic acid in a side reaction, see Figure 8.

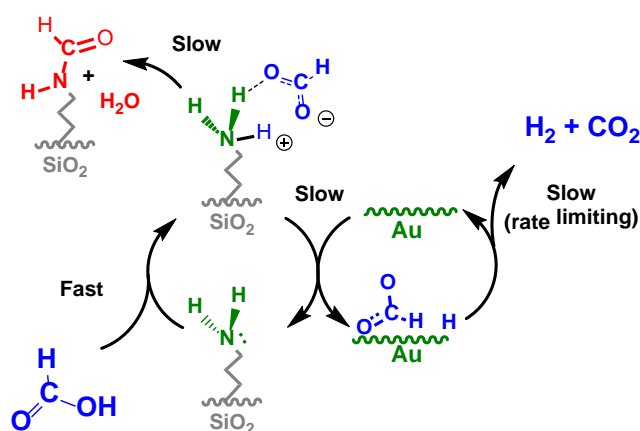


Figure 8. Simplistic overview of the dual cycle amine-Au mechanism for formic acid decomposition. The off-cycle deactivation of amine adsorption sites is shown in red.

It has previously been shown that the rate of HCOOH decomposition over Au nanoparticles may be significantly increased in the presence of an amine [10]. The irreversible blockage of amine sites due to amide formation therefore offers a good explanation for the initial deactivation discussed earlier (see supporting information S6-S7). The key function of the amine is to facilitate OH bond cleavage, which leads to the formation of Au-formate species. The Au-formate species may then undergo further dehydrogenation and react with the protonated amine to give H_2 along with CO_2 via a β -elimination pathway [12]. We therefore propose that the irreversible formation of formamide may decrease the reaction rate by decreasing the number of silica grafted amine groups, which functions as

effective deprotonation sites under mild reaction conditions. The formation of the proposed amide species is shown in red in Figure 8 along with a simplistic overview of the proposed mechanism.

The kinetics of the relative amide formation was investigated by extracting the absorbance of the amide $\nu_{\text{C=O}}$ using a Gaussian deconvolution methodology described in our previous work [26]. The resulting kinetic profiles are shown in Figure 9.

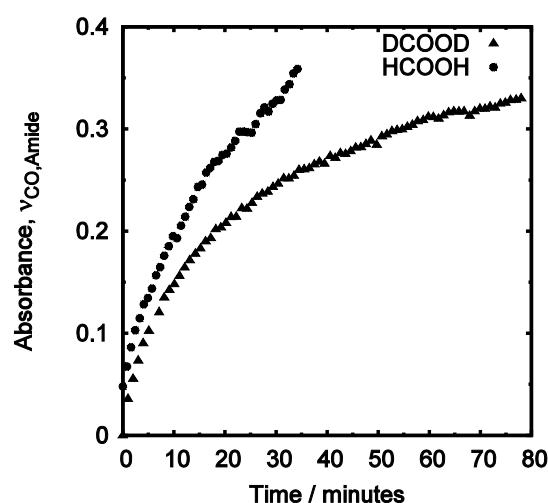


Figure 9. Formation of the amide species during HCOOH and DCOOD exposure of on the core-shell Au@SiO_2 2.2 ± 0.3 catalysts at 120°C . The integrated absorbance is derived from the deconvoluted difference spectra of the 1665 cm^{-1} and 1635 cm^{-1} bands, respectively

Figure 9 shows how the rate of amide formation with HCOOH and DCOOD was almost identical in the beginning of the experiment. After 10 min, however, the rates started to deviate and a strong kinetic isotope effect became evident. We believe that the kinetic isotope effect may be explained by the need for breaking two amine N-D bonds, while the similar rates during the first 10 min may be explained by the high H content in the beginning of the experiment.

After around 40 min of exposure (80 min for the DCOOD experiment) the flow was switched to

pure N₂ gas in order to study the conversion of the absorbed formic acid species and discriminate the reactive surface species from nonreactive, see Figure 11. These experiments showed that the species associated with absorbed protonated formic acid (peak at 1725 cm⁻¹) disappeared faster than the formate species (see supporting information).

In general, the formate species were converted by a first order type reaction (see peaks at 1577/1575 cm⁻¹ and 1360/1325 cm⁻¹, respectively). We therefore used the deconvolution methodology, which allowed us to determine the kinetic profiles of this reaction. Figure 10 shows a logarithmic plot of these profiles.

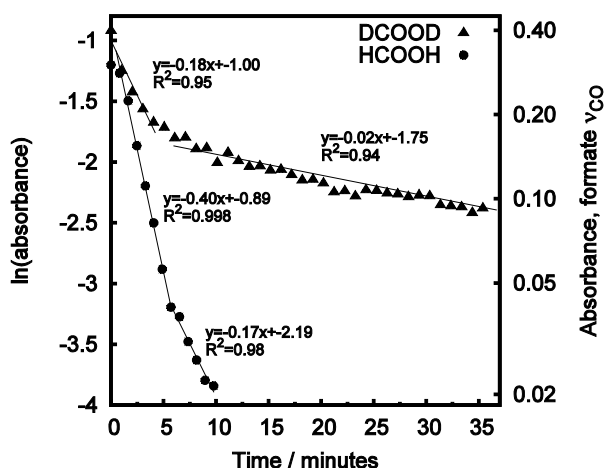


Figure 10. Conversion of adsorbed formate species based on the integrated absorbance of the deconvoluted spectra during N₂ flushing of Au@SiO₂ 2.2±0.3 pre-saturated with HCOOH for 40 min and DCOOH for 80 min at 120°C.

The data in Figure 10 shows that a large part of the formate species (~85%) was converted by a first order reaction. It appears that the adsorption and transfer to the Au site occurs relatively fast, while the subsequent decomposition of HCOO⁻ is rate-limiting. The remaining part of the formate (~15%) was converted at a lower rate, which indicate that the conversion becomes controlled by internal diffusion. By estimation, the ratio of amine used in the synthesis and the amount of surface gold atoms is roughly 13:1. This indicate that the catalyst has a large number of amine adsorptions sites, from where the HCOO⁻ species can diffuse to an active gold site.

The kinetic profile for the DCOO⁻ conversion deviated significantly from the HCOO⁻ profile. The first half of the DCOO⁻ species was converted with a first order rate constant, which was around 45% of that for HCOO⁻. The remaining half of the DCOO⁻ species were converted at a significantly lower rate. In a control experiment we investigated the same effect on a fresh catalyst. By switching between DCOOH/N₂ and pure N₂, we found that that the difference between the DCOO⁻ and HCOO⁻ reaction rates was less pronounced with a fresh catalyst with almost no amide species (see details described in supporting information, including Figure S17 and Table S1).

The peak at 1665 cm⁻¹ was stable over time, which confirmed our assignment as a nonreactive species. Figure 11 showed that more clearly resolved bands became visible after the formate species were removed. Based on DFT calculations, the bands at 1525 cm⁻¹ and 1387 cm⁻¹ further supports the structure of the proposed amide species.

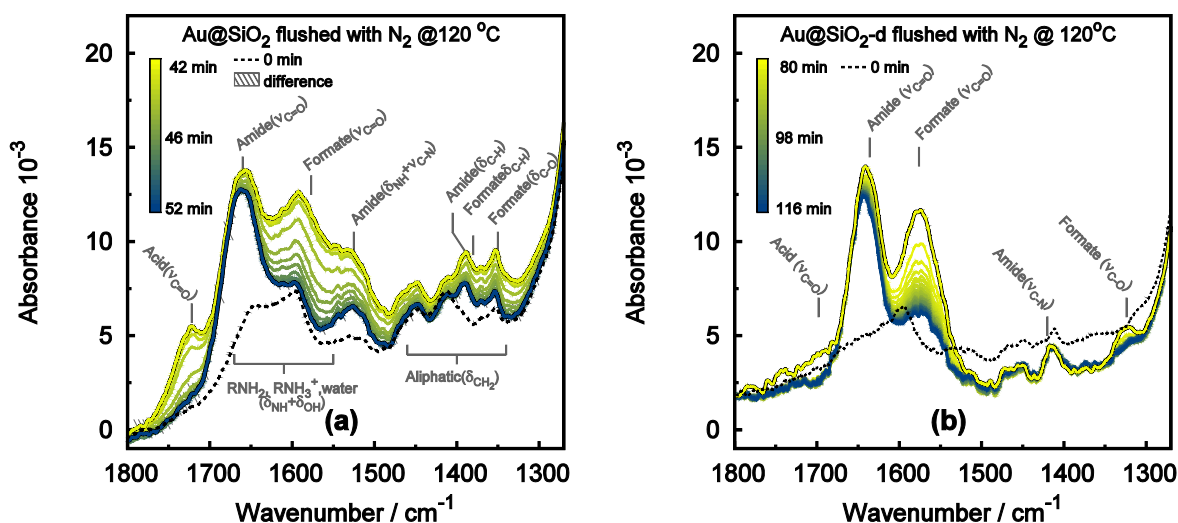


Figure 11. *In situ* ATR-FTIR spectra continuing experiments in Figure 7, where the formic acid saturated Au@SiO₂ 2.2±0.3 catalyst was flushed with nitrogen at 120°C. The spectra are coloured with a gradient indicating time since experiment started (see Figure 7). Initial yellow spectra are indicated by a black outline. a) The flushing of the formic acid saturated catalyst with N₂, initial spectrum recorded prior to formic acid vapour exposure is shown for comparison. The hatched area on (a) shows the difference between the fresh and used catalyst, thus indicating the features on the amide species.

4 Conclusion

Gold nanoparticles encapsulated in silica are highly active catalysts for the production of hydrogen by vapour phase decomposition of formic acid. The Au@SiO₂ core-shell catalysts were prepared in a reverse micelle system that made it possible to control the particle size distribution and shell thickness, which have a large impact on the catalytic activity. The smallest gold nanoparticles were 2.2±0.3 nm in diameter and afforded a TOF of up to 958 h⁻¹ at a temperature of 130°C. The remarkable particle size effect on the TOFs and the results from *in situ* ATR-FTIR spectroscopy indicate that the reaction occurs by a dual site mechanism involving an amine absorption site and a low-coordinated Au atom, while results from kinetic isotope labelling experiments indicate that H-assisted formate decomposition into CO₂ and H₂ is the rate limiting step. The observed deactivation could be related to the formation of inactive amide species in an off-cycle reaction between the amine and formic acid. The study therefore suggests that

the design of a more stable amine absorption site could improve the catalytic activity over time. In conclusion, the reverse micelle method is simple, practical and results in a narrow size distribution of small nanoparticles that are encapsulated by a thin shell of silica that remain accessible to formic acid. By optimisation of the amine adsorption site and the active metal composition to improve the selectivity we therefore expect that silica encapsulated metal nanoparticles may find use for activation of formic acid for future renewable energy or chemical processes.

5 Acknowledgements

The authors gratefully acknowledge the support of the Danish Council for Independent Research, Grant No. 12-127580, the support of the Lundbeck Foundation (Lundbeckfonden), Grant No. R141-2013-13244 and the support from VILLUM FONDEN research grant (13158).

6 References

- [1] S. Moret, P.J. Dyson, G. Laurenczy, Direct synthesis of formic acid from carbon dioxide by hydrogenation in acidic media, *Nat. Commun.* 5 (2014) 1–7. doi:10.1038/ncomms5017.
- [2] R. Wölfel, N. Taccardi, A. Bösmann, P. Wasserscheid, Green Chemistry Selective catalytic conversion of biobased carbohydrates to formic acid using molecular oxygen †, *Green Chem.* 13 (2011) 2759–2763. doi:10.1039/c1gc15434f.
- [3] M.J. Gilkey, B. Xu, Heterogeneous Catalytic Transfer Hydrogenation as an Effective Pathway in Biomass Upgrading, *ACS Catal.* 5 (2016) 1420–1436. doi:10.1021/acscatal.5b02171.
- [4] S. Kegnæs, J. Mielby, U. V. Mentzel, C.H. Christensen, A. Riisager, Formation of imines by selective gold-catalysed aerobic oxidative coupling of alcohols and amines under ambient conditions, *Green Chem.* 12 (2010) 1437. doi:10.1039/c0gc00126k.
- [5] S. Kegnæs, J. Mielby, U. V. Mentzel, T. Jensen, P. Fristrup, A. Riisager, One-pot synthesis of amides by aerobic oxidative coupling of alcohols or aldehydes with amines using supported gold and base as catalysts, *Chem. Commun.* 48 (2012) 2427. doi:10.1039/c2cc16768a.
- [6] J. Mielby, J.O. Abildstrøm, F. Wang, T. Kasama, C. Weidenthaler, S. Kegnæs, Oxidation of bioethanol using zeolite-encapsulated gold nanoparticles, *Angew. Chemie - Int. Ed.* 53 (2014) 12513–12516. doi:10.1002/anie.201406354.
- [7] M. Haruta, N. Yamada, T. Kobayashi, S. Iijima, Gold Catalysts Prepared by Coprecipitation for Low-Temperature Oxidation of Hydrogen and of Carbon Monoxide, *J. Catal.* 115 (1989) 301–309.
- [8] J. Mielby, S. Kegnæs, P. Fristrup, Gold Nanoparticle-Catalyzed Formation of Nitrogen-containing Compounds-From Mechanistic Understanding to Synthetic Exploitation, *ChemCatChem.* 4 (2012) 1037–1047. doi:10.1002/cctc.201200314.
- [9] N. Lopez, T.V.W. Janssens, B.S. Clausen, Y. Xu, M. Mavrikakis, T. Bligaard, et al., On the origin of the catalytic activity of gold nanoparticles for low-temperature CO oxidation, *J. Catal.* 223 (2004) 232–235. doi:10.1016/j.jcat.2004.01.001.
- [10] Q. Bi, X. Du, L. He, Y. Liu, Y. Cao, H. He, et al., Efficient Subnanomeric Gold-Catalyzed Hydrogen Generation from Formic Acid Decomposition under Ambient Conditions **, *J. Am. Chem. Soc.* 134 (2012) 8926–8933. doi:10.1002/anie.2001).
- [11] M. Yadav, T. Akita, N. Tsumori, Q. Xu, Strong metal – molecular support interaction (SMMSI): Amine-functionalized gold nanoparticles encapsulated in silica nanospheres highly active for catalytic decomposition of formic acid, *J. Mater. Sci.* 22 (2012) 12582–12586. doi:10.1039/c2jm31309j.
- [12] M. Ojeda, E. Iglesia, Formic Acid Dehydrogenation on Au-Based Catalysts at Near- Ambient Temperatures, *Angew. Chem. Int. Ed. Engl.* 121 (2009) 4894–4897. doi:10.1002/ange.200805723.
- [13] D.A. Bulushev, S. Beloshapkin, J.R.H. Ross, Hydrogen from formic acid decomposition over Pd and Au catalysts, *Catal. Today.* 154 (2010) 7–12. doi:10.1016/j.cattod.2010.03.050.
- [14] A. Gazsi, T. Bánsági, F. Solymosi, Decomposition and Reforming of Formic Acid on Supported Au Catalysts : Production of CO-Free H₂, *J. Phys. Chem. C.* 115 (2011) 15459–15466.
- [15] A. Gallas-Hulin, J. Mielby, S. Kegnaes, Efficient Production of Hydrogen from Decomposition of Formic Acid over Zeolite Incorporated Gold Nanoparticles, *ChemistrySelect.* 1 (2016) 3942–3945. doi:10.1002/slct.201600831.
- [16] a Herron, J. Scaranto, P. Ferrin, S. Li, M. Mavrikakis, Trends in Formic Acid Decomposition on Model Transition Metal Surfaces : A Density Functional Theory study, *ACS Catal.* 4 (2014) 4434–4445.
- [17] J.S. Yoo, F. Abild-pedersen, J.K. Nørskov, F. Studt, Theoretical Analysis of

- Transition-Metal Catalysts for Formic Acid Decomposition, *ACS Catal.* 4 (2014) 1226–1233.
- [18] T. Zhang, H. Zhao, S. He, K. Liu, H. Liu, Y. Yin, et al., Unconventional route to encapsulated ultrasmall gold nanoparticles for high-temperature catalysis, *ACS Nano.* 8 (2014) 7297–7304. doi:10.1021/nn502349k.
- [19] A.J. Kunov-Kruse, J. Thomsen, J. Piltoft, C. Petersen, Patent application EP12174778.6, 2012.
- [20] A. Rimola, D. Costa, M. Sodupe, J.-F. Lambert, P. Ugliengo, Silica Surface Features and Their Role in the Adsorption of Biomolecules : Computational Modeling and Experiments, *Chem. Rev.* 113 (2013) 4216–4313.
- [21] M. Zacharska, A.L. Chuvilin, V. V. Kriventsov, S. Beloshapkin, M. Estrada, A. Simakov, et al., Support effect for nanosized Au catalysts in hydrogen production from formic acid decomposition, *Catal. Sci. Technol.* 6 (2016) 6853–6860. doi:10.1039/C6CY00552G.
- [22] G. Ertl, H. Knozinger, F. Schüth, J. Weitkamp, eds., *Handbook of Heterogeneous Catalysis*, 2nd Ed., Wiley-VCH, Weinheim, Germany, 2008.
- [23] N. Lopez, On the origin of the catalytic activity of gold nanoparticles for low-temperature CO oxidation, *J. Catal.* 223 (2004) 232–235. doi:10.1016/j.jcat.2004.01.001.
- [24] T.V.W. Janssens, B.S. Clausen, B. Hvolbæk, H. Falsig, C.H. Christensen, T. Bligaard, et al., Insights into the reactivity of supported Au nanoparticles: Combining theory and experiments, *Top. Catal.* 44 (2007) 15–26. doi:10.1007/s11244-007-0335-3.
- [25] K.T. Queeney, N. Herbots, J.M. Shaw, V. Atluri, Y.J. Chabal, Infrared spectroscopic analysis of an ordered Si/SiO₂ interface, *Appl. Phys. Lett.* 84 (2004) 493–495. doi:10.1063/1.1644030.
- [26] S. Saravanamurugan, A.J. Kunov-kruse, R. Fehrmann, A. Riisager, Amine-Functionalized Amino Acid-based Ionic Liquids as Efficient and High-Capacity Absorbents for CO₂, *ChemSusChem.* 7 (2014) 897–902. doi:10.1002/cssc.201300691.